PCCP

PAPER

Cite this: *Phys. Chem. Chem. Phys.*, 2016, **18**, 27967

Mechanistical investigation on the self-enhanced photocatalytic activity of CuO/Cu_2O hybrid nanostructures by density functional theory calculations

Feiyu Diao, FengHui Tian,* Wenshuang Liang, Honglei Feng and Yiqian Wang*

Received 8th June 2016,
Accepted 14th September 2016

DOI: 10.1039/c6cp03977d

www.rsc.org/pccp

The photocatalytic mechanism of a Cu_2O/CuO hybrid system is disclosed in detail by density functional theory (DFT) calculations. The synergistic relationship of the two counterparts is confirmed by hydrogen peroxide (H_2O_2) formation on the CuO nanowires and dissociation on the Cu_2O nanoparticles; this enables the system to self-sufficiently produce hydroxyl radicals, which is highly efficient in the photocatalytic degradation of methyl orange. The exposed surfaces are found to be crucial in the cooperative photocatalytic system, especially the Cu_2O(111) surface, in the dissociation of H_2O_2. The distinct positions of the conduction band minimum and valence band maximum for CuO and Cu_2O and synergic surface reactions enable the effective utilization of the electrons and holes generated by visible-light irradiation. Our results will contribute to a greater understanding of the specific mechanism of photodegradation catalyzed by Cu_2O/CuO heterostructures, which may lead to promising directions in structure optimization for photocatalysts with high photocatalytic efficiency.

1. Introduction

Growing concerns worldwide regarding environmental water have strongly stimulated the pursuit of efficient and green treatments of organic pollutants, such as metallic oxide photocatalysts.[1–3] Extensively studied wide-bandgap semiconductors such as TiO_2 and ZnO,[4,5] in spite of their good photostability and high catalytic efficiency, are limited by the narrow ultraviolet range of their irradiation light.[6] Therefore, narrow-bandgap semiconductors such as CuO and Cu_2O have drawn intensive research interest; however, their poor photostability and relatively fast recombination of photogenerated charge carriers severely limit their practical utilization.[7] At present, considerable efforts have been devoted towards designing catalysts with desired compositions and structures to improve photocatalytic efficiency.[8] Recently, novel efficient heterogeneous photocatalysts such as TiO_2/CuO,[9] CuO/CeO_2[10] and Cu_2O/CuO[11,12] have been widely studied. In particular, Cu_2O/CuO heterostructures have shown fairly good application prospects in the field of photocatalysis because of their favorable band alignments for the effective separation of photogenerated charge carriers.[7] In addition, the abundance of copper resources in nature enables the large-scale fabrication of Cu_2O/CuO based photocatalysts.

College of Physics & The Cultivation Base for State Key Laboratory, Qingdao University, No. 308, Ningxia Road, Qingdao, 266071, P. R. China. E-mail: tfh@qdu.edu.cn, yqwang@qdu.edu.cn; Tel: +86-532-85950690, +86-532-83780318

For photocatalysts, in addition to the optimization of their compositions and structures, the role of specific exposed surfaces in the photocatalytic process deserves special attention. Surface atomic/electronic structures, dangling bonds, and crystal defects have been confirmed to be critical for photocatalytic performance.[13] It has been demonstrated that the most promising route to improve this performance is to increase the density of the most active facets in nanophotocatalysts.[14] Therefore, the design of efficient photocatalysts includes not only the selection of proper components but also the rational arrangement of the active sites in the photocatalysts. However, a comprehensive understanding of the synergistic mechanism in heterogeneous photocatalysts, especially imperceptible surface reactions and the migration of charge carriers, is still lacking. Computational modeling can help to elucidate the detailed reaction processes occurring on the surfaces of individual components which cannot be directly experimentally observed; this can then provide assembly principles for the design of new materials.

Furthermore, it has been widely accepted that adding a sufficient amount of hydrogen peroxide (H_2O_2) to a photocatalytic system will significantly enhance its photocatalytic efficiency.[15–17] For example, the photocatalytic capacity of Cu_2O has been increased more than fifteen-fold[18] in the degradation of methyl orange (MO) by the addition of H_2O_2. The enhanced photocatalytic activity is usually attributed to the photoreactive oxidant radicals (such as $^{\bullet}O^{2-}$ and $^{\bullet}OH$) formed in the reduction process of H_2O_2, induced by photocatalysts.[19] Recently, we reported a

novel hybrid nanocomposite of polyhedral Cu_2O nanoparticles (NPs)/CuO nanowires (NWs)[20] with excellent photocatalytic performance in visible light which is even comparable to that of TiO_2 under ultraviolet irradiation[21] without introduction of H_2O_2. In view of the H_2O_2 production ability of CuO[22] and the excellent photocatalytic ability of Cu_2O[18] in the presence of H_2O_2, we proposed a photocatalytic mechanism[20] where the synergistic effect of the formation of H_2O_2 on CuO and the dissociation of H_2O_2 on Cu_2O greatly improves the efficiency of MO degradation. However, the corresponding surface reactions and interface migrations of electrons and holes are still unknown. A theoretical simulation may provide credible answers.

The purpose of the present work is to provide a fundamental understanding of the overall photocatalytic mechanism of heterogeneous catalysts. Taking Cu_2O/CuO hybrid nanostructures as an example, the complicated chemical nature of the synergic effects in a heterogeneous photocatalytic system is investigated by DFT calculations. We focus on the different roles of individual Cu_2O NPs and CuO NWs in the increased production of oxidant radicals. Based on the Cu_2O/CuO hybrid nanostructures, we build theoretical models to investigate the interplay of crystal surfaces and the species in solution. It is shown that H_2O_2 is generated by the storage of O_2 on CuO, and the formation of $^{\bullet}OH$ species mainly occurs on Cu_2O, particularly on the Cu_2O(111) surfaces. The generation and dissociation of H_2O_2 promotes the circular migration of generated electrons and holes and efficiently suppresses their recombination. The photocatalytic mechanism disclosed in this study will provide desirable design principles for more efficient photocatalysts.

2. Computational methods

All calculations in the present work were carried out using the DMol^3 program package in Material Studio.[23,24] The Perdew–Burke–Ernzerhof (PBE) model of generalized gradient approximation (GGA) was used as the exchange–correlation function.[25] The valence orbitals of the atoms were described by setting the double-numeric quality with polarization functions (DNP), and DFT semi-core pseudopotentials (DSPPs) were utilized to substitute the core electrons.[26,27] The convergence criterion of the energy, force and displacement for optimized configurations were 2.0×10^{-5} Ha per atom, 0.004 Ha Å^{-1} and 0.005 Å, respectively. A Methfessel–Paxton smearing of 0.01 Ha was used to improve the calculation performance. Periodic (2×2) slab models with three O–Cu–O layers were used to simulate the Cu_2O(111), (100) and (110) surfaces, and (3×2) slab models with two O–Cu–O layers were used to simulate the CuO (111), (311) and (202) surfaces. The adsorption energy (E_{ads}) was calculated using the following equation:[28,29]

$$E_{ads} = E_{adsorbate} + E_{surface} - E_{adsorbate/surface} \quad (1)$$

where $E_{adsorbate}$ is the energy of isolated adsorbed species in the vacuum, $E_{surface}$ is the energy of the Cu_2O or CuO surface and $E_{adsorbate/surface}$ is the total energy of the surface with the adsorbed species. According to this equation, a positive value of E_{ads} corresponds to an energetically favorable adsorption process.

3. Results and discussion

The structures of the Cu_2O and CuO crystals and the main adsorbed species (O_2 and H_2O_2) were optimized to verify the accuracy of our calculation methods. As shown in Table 1, the lattice parameters of cubic Cu_2O and monoclinic CuO and the bond lengths of O_2 and H_2O_2 used in this work are consistent with theoretical and experimental values in previous reports.[30–39]

3.1 The generation of $^{\bullet}OH$

DFT calculations were carried out to clarify the different roles of CuO and Cu_2O in the hybrid photocatalytic system. Because the active oxidant radicals are directly related to the photocatalytic efficiency, the generation of $^{\bullet}OH$ radicals was investigated first by calculating the H_2O_2 adsorption on different surfaces of the CuO NWs and Cu_2O NPs in the CuO/Cu_2O hybrid system. The (111) and (100) facets exposed in the octahedral and cubic Cu_2O NPs were confirmed by HRTEM observations.[20] Rahman *et al.*[40] have theoretically demonstrated that the O-terminated Cu_2O(100) surface is preferred over the Cu-terminated surface within the entire range of pressures and temperatures. Herein, the O-terminated Cu_2O(100) surface was optimized for the adsorption of H_2O_2. In addition, the (110) surface of Cu_2O, which is generally regarded as a highly reactive facet,[41] was also considered. For CuO NWs, most exposed surfaces are expected to be high-index surfaces; thus, we chose two representative high-index surfaces, (311) and (202), based on vast statistical data from XRD results.[42–44] In addition to the high-index surfaces, the stable CuO(111) surface is also investigated to give a more comprehensive explanation. Fig. 1 shows the most stable configurations of H_2O_2 adsorbed on different surfaces obtained by optimizing several possible adsorption geometries of each surface. Table 2 presents the corresponding geometric parameters and adsorption energies. From these geometrical configurations, it can be found that the H_2O_2 molecule is only dissociated on the Cu_2O(111) surface. Moreover, it is interesting to note that only one stable hydroxylation configuration forms on the Cu_2O(111) surface with no constraints, which results from the dissociation of H_2O_2, as shown in Fig. 1a. After optimization,

Table 1 Comparison of the calculated structure parameters with previous studies for adsorbates and substrates

System	Parameter	This work	References		Experimental
O_2	d_{OO} (Å)	1.226	1.224[30]	1.270[31]	1.236[32]
H_2O_2	d_{OO} (Å)	1.469	1.455[33]	1.453[31]	1.455[34]
	d_{OH} (Å)	0.976	0.974[33]	0.966[31]	0.967[34]
	d_{OH} (Å)	0.976	0.974[33]	0.966[31]	0.967[34]
Cu_2O	a (Å)	4.269	4.300[35]	4.277[36]	4.27[37]
CuO	a (Å)	4.653	4.758[30]	4.683[38]	4.683[39]
	b (Å)	3.410	3.415[30]	3.430[38]	3.422[39]
	c (Å)	5.108	5.167[30]	5.138[38]	5.129[39]
	β	99.50	99.57[30]	99.20[38]	99.54[39]

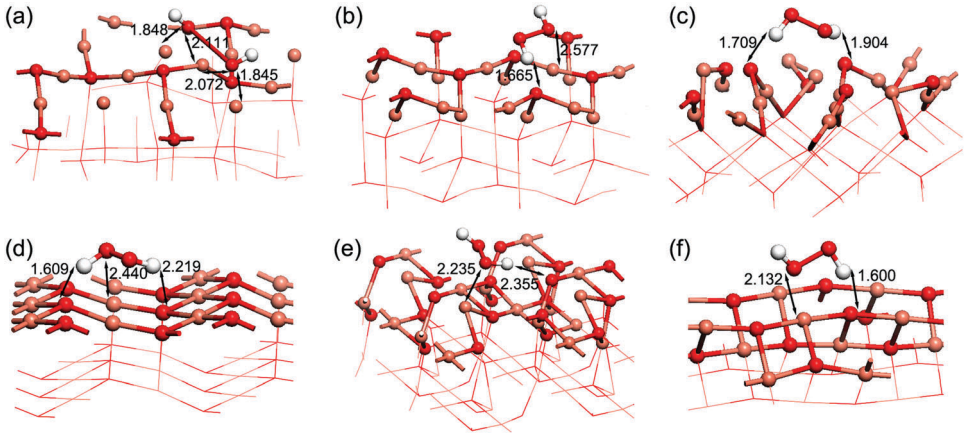

Fig. 1 Optimized adsorption configurations of H_2O_2 on different surfaces. (a) $Cu_2O(111)$; (b) $Cu_2O(110)$; (c) $Cu_2O(100)$; (d) CuO(111); (e) CuO(311); and (f) CuO(202). The bond lengths are given in Å.

Table 2 Properties of H_2O_2 adsorption configurations on different surfaces

Model		ΔE^a (eV)	Δq^b (e)	Products on surface	Bond lengths (Å) in product			Torsion[c]
					O–O	O–H	O–H	
Free H_2O_2					1.469	0.977	0.976	110.8
Cu_2O	(111)	4.27	−0.487	2 •OH	3.748	0.975	0.974	
	(110)	0.60	0.164	H_2O_2	1.468	1.013	0.979	143.7
	(100)	2.20	0.091	H_2O_2	1.459	1.006	0.991	28.7
CuO	(111)	0.60	0.199	H_2O_2	1.471	1.026	0.986	158.8
	(311)	0.70	0.135	H_2O_2	1.476	0.979	0.991	112.8
	(202)	0.82	0.142	H_2O_2	1.483	1.030	0.979	175.1
$Cu_2O(111)$ (fixed)	*a*	1.31	0.147	H_2O_2	1.513	0.981	1.010	106.8
	b	4.53	−0.476	2 •OH	3.794	0.971	0.974	
	c	2.80	−0.595	H_2O + O	2.770	0.971[d]	0.992[d]	

[a] ΔE means the calculated adsorption energies. [b] Δq is the charge transferred from the H_2O_2 molecule to the surface. [c] Torsion is the H–O═O–H torsion angle in the H_2O_2 molecule. [d] 0.971 and 0.992 Å are the O–H bond lengths in the formed H_2O molecule.

the O–O bond in H_2O_2 is broken due to electrostatic interactions with the two adjacent Cu_{1C} surface atoms, with a bond length elongated from 1.468 Å to 3.748 Å. To clarify the products of dissociated H_2O_2, we calculated the stretching frequencies of two separate O–H bonds. The calculated frequencies (3666 and 3684 cm^{-1}) of the OH bending vibration are close to the experimental frequency (3740 cm^{-1}) of •OH radical[45] and are far away from the vibration frequency (3296 cm^{-1}) of OH^- ion[46]. The spin density shown in Fig. 2 and the magnetic moments displayed in Table 3 demonstrate the existence of unpaired electrons in the optimized system, indicating that the main dissociation products of H_2O_2 on the $Cu_2O(111)$ surface are •OH radicals. However, the magnetic moments for the formed OH species on $Cu_2O(111)$ are smaller than those of the free •OH radicals, suggesting that the formed •OH radicals may be partially reduced during the adsorption process. Previous experimental results[47,48] have also shown that the catalytic decomposition of H_2O_2 on metal oxide surfaces involves the homolytic cleavage of the O–O bond in H_2O_2 to form two •OH radicals, which is in good agreement with our calculated results. However, in the adsorption configurations on the $Cu_2O(110)$, (100) and CuO(111), (311) and (202) surfaces, as shown in Fig. 1b–f, the adsorbed

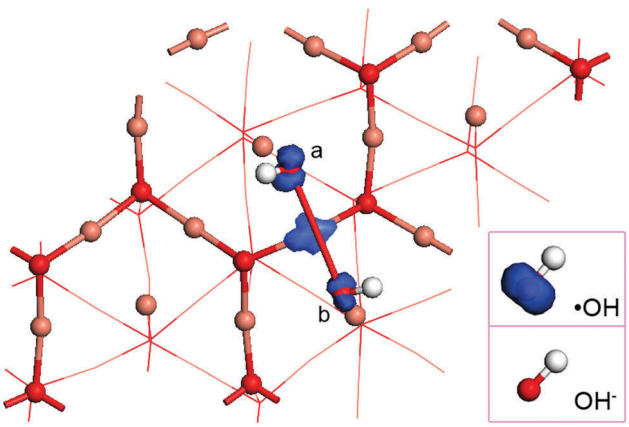

Fig. 2 Spin density of OH species on the $Cu_2O(111)$ surface, •OH radical and OH^- ion.

H_2O_2 molecules are not dissociated but are slightly distorted. The distortions of H_2O_2 molecules originated from the slightly elongated O–H bond lengths and the drastic change in the H–O═O–H torsion angles. The detailed geometric parameters are displayed in Table 2. The distorted H_2O_2 molecules are

Table 3 Magnetic moments of O and H atoms in •OH, OH^- and OH species on the $Cu_2O(111)$ surface

		OH species on $Cu_2O(111)$[a]		
Atom	•OH	*a*	*b*	OH^-
O	1.015	0.032	0.021	0.000
H	−0.015	0.000	0.001	0.000

[a] The two OH species on the $Cu_2O(111)$ surface are marked *a* and *b*, as displayed in Fig. 2.

adsorbed mainly through hydrogen bonds formed between the H atoms of H_2O_2 and the surface oxygen atoms. The calculated adsorption energies for H_2O_2 on the six listed surfaces [$Cu_2O(111)$, (110), (100) and CuO(111), (311) and (202) surfaces] are 4.27, 0.60, 2.20, 0.60, 0.70 and 0.82 eV, respectively. The highest adsorption energy of H_2O_2 on the $Cu_2O(111)$ surface confirms that the H_2O_2 dissociation is the most stable configuration. The adsorption energies for the CuO(311) and (202) surfaces are slightly larger than that for the CuO(111) surface. Except for this, no remarkable differences can be found between the two cases of CuO high-index and low-index surfaces. H_2O_2 molecules cannot be dissociated on CuO surfaces, even on the high-index surfaces. Thus, the dissociation process of H_2O_2 on the $Cu_2O(111)$ surface governs the generation of •OH radicals. Furthermore, it should be noted that the surface Cu_{1C} site is only found on the $Cu_2O(111)$ surface in the above-mentioned six surfaces. Therefore, the surface Cu_{1C} site is crucial for the dissociation of H_2O_2 as well as for the formation of •OH.

Yu *et al.*[12] reported that a composite of CuO and Cu_2O could enhance photocatalytic activity for the decolorization of MO under visible-light illumination. However, the enhanced photocatalytic efficiency (only 12%) of CuO/Cu_2O composite hollow microspheres[12] is far lower than that (up to 67.1%) of Cu_2O NPs/CuO NWs hybrid nanostructures.[20] In order to determine the reason for this enormous gap between the photocatalytic efficiencies of the two CuO/Cu_2O composite materials, the morphologies and microstructures of the two materials were compared in detail. It was found that the essential distinction between the structures of the two hybrid materials is the exposed surface of the Cu_2O component. Statistical analysis shows that 80% Cu_2O NPs in the Cu_2O NPs/CuO NWs hybrid nanostructures are nanooctahedra with a high exposure rate of $Cu_2O(111)$ surfaces, while similar structures cannot be found in the CuO/Cu_2O composite hollow microspheres. Meanwhile, our calculated results illustrate the key role of the $Cu_2O(111)$ surface in the dissociation process of H_2O_2, which corroborates the experimental observations. Both the calculated and experimental results suggest that the most significant factor for enhanced photocatalytic activity is extensive exposure of the $Cu_2O(111)$ surfaces. In addition, the intuitive size differences between the two CuO/Cu_2O composites play an important role in the enhanced photocatalytic activity. The CuO/Cu_2O composite hollow microspheres (500 nm to 5 μm) are much larger than the hybrid nanostructures composed of Cu_2O NPs (~50 nm) and CuO NWs (100 nm). From the optimized configurations shown in Fig. 1, the structural relaxation effects on the Cu_2O slabs are found to be more significant than on the CuO slabs, which indicates that the influence of size on both the structures and properties of Cu_2O is quite noteworthy. The optimized configurations of H_2O_2 adsorbed on unconstrained $Cu_2O(111)$ slabs reflect the reactions occurring on the Cu_2O nanooctahedra. To compare the activities of bulk and nanoscale Cu_2O, we modified the $Cu_2O(111)$ slab by fixing the bottom O–Cu–O layer to the bulk Cu_2O coordinates.

From above, it can be seen that for the unfixed $Cu_2O(111)$ surface, only •OH species are produced after the adsorption of H_2O_2. However, for the fixed $Cu_2O(111)$ surface, three final configurations are obtained after optimization, as shown in Fig. 3. In the configuration shown in Fig. 3a, the H_2O_2 molecules are slightly distorted; in the other two configurations in Fig. 3b and c, the H_2O_2 molecules are dissociated into two •OH species and into H_2O and O species, respectively. Diversification of the dissociated products on the fixed $Cu_2O(111)$ surface decreases the chance of •OH generation through the dissociation of H_2O_2. Furthermore, although •OH species can also be generated on the fixed $Cu_2O(111)$ surface, the surface Cu_{1C} atoms are distended severely, as shown in Fig. 3b. One Cu–O surface bond is broken, with the bond length elongated from 1.895 to 3.246 Å, which indicates that the crystal surface in bulk Cu_2O will be heavily damaged when the •OH species are produced. Thus, the reutilization and stability of the photocatalysts will be inevitably affected. This is confirmed from the perspective that nanomaterials usually show better photocatalytic activities than bulk materials.

In addition to the dissociation of H_2O_2 molecules, the •OH species can also be generated through the adsorption of OH^- ions on Cu_2O surfaces. Our calculated stretching frequency (3689 cm^{-1}) of the adsorbed OH^- ions on the $Cu_2O(111)$ surface is much closer to the observed vibrational frequency (3740 cm^{-1}) of the •OH species,[45] which confirms the transformation of OH^- ions into •OH radicals. Thus, the formation of •OH radicals mainly occurs on Cu_2O NPs through the dissociation of H_2O_2 and the transformation of OH^- ions.

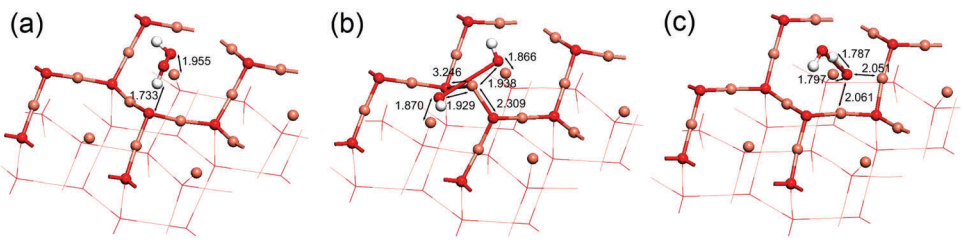

Fig. 3 Three products of H_2O_2 adsorbed on a fixed $Cu_2O(111)$ surface. (a) H_2O_2; (b) 2•OH; (c) H_2O + O. The bond lengths are given in Å.

3.2 The source of H_2O_2

Just as confirmed in our previous report,[20] the Cu_2O/CuO hybrid photocatalytic system showed excellent photocatalytic efficiency without introducing H_2O_2. Thus, two questions arise. What do CuO NWs contribute to the hybrid photocatalytic system, apart from being an electron acceptor? Is H_2O_2 self-generation catalyzed by CuO? These questions led us to explore the source of H_2O_2 and the reactions occurring on the CuO NWs. Based on the assumptions in a previous report,[22] the reactions in the formation process of H_2O_2 include two steps: the activation of O_2 and the interactions between the activated O_2 and H^+ ions. The H^+ ions in water exist in the form of hydronium ions (H_3O^+);[49] accordingly, in the present work, the H^+ ions are modeled as H_3O^+. Considering the unique morphology of the nanowires, the formation processes of H_2O_2 are simulated on both the low-index and high-index facets.

For the low-index surface, the relatively high adsorption energy (4.69 eV) for the adsorption of H_3O^+ indicates that the CuO(111) surfaces are readily hydrogenated. Thus, the H_2O_2 formation processes on both clean and hydrogenated (111) surfaces were investigated, and the simulated results are displayed in Fig. 4. The corresponding geometric parameters and adsorption energies are summarized in Tables 4 and 5, respectively. A final point to address is that the hydrogenated CuO(111) surface is more favorable for the formation of H_2O_2 than the clean CuO(111) surface. Regarding O_2 adsorption, on both the clean and hydrogenated CuO(111) surfaces, as shown in Fig. 4a and c, the parallel configurations with O_2 bonded to two adjacent Cu_{3C} atoms are found to be the most stable adsorption structures, which is in good agreement with the calculated results reported by Sun *et al.*[30] The adsorbed O_2 molecules are activated and transformed into O_2^- ions. The O–O bond lengths of activated O_2^- ions on the clean and hydrogenated surfaces are elongated to 1.313 Å and 1.351 Å; the adsorption energies for O_2 activated on the clean and hydrogenated surfaces are 0.72 eV and 1.06 eV; and the charges transferred from the clean and hydrogenated surfaces to O_2 are 0.225 *e* and 0.409 *e*, respectively.

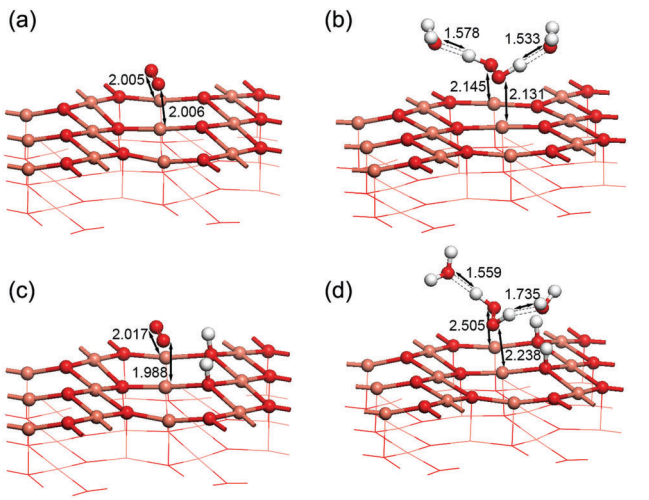

Fig. 4 Formation process of H_2O_2 on CuO(111) surfaces. The activation of O_2 on clean (a) and hydrogenated (c) surfaces. The final products on clean (b) and hydrogenated (d) surfaces. The bond lengths are given in Å.

Table 4 Calculated geometric parameters for activated O_2^- ions and formed H_2O_2 on CuO surfaces

Model		Bond lengths (Å) in adsorbed species O–O	O–H	O–H	Torsion[a]
Clean(111)	O_2^-	1.313	1.031	1.044	123.8
	H_2O_2	1.469			
Hydrogenated(111)	O_2^-	1.351	1.033	1.005	102.9
	H_2O_2	1.468			
(311)	O_2^-	1.331	1.038	1.188	73.4
	H_2O_2	1.470			
(202)	O_2^-	1.319	1.033	1.037	117.7
	H_2O_2	1.474			

[a] Torsion is the H–O═O–H torsion angle in the formed H_2O_2 molecule.

Table 5 Adsorption energies for adsorbates on CuO surfaces. The energies are given in eV

Adsorbate/surface	Clean(111)	Hydrogenated(111)	(311)	(202)
H_3O^+	4.69		2.35	3.41
O_2	0.72	1.06	2.25	2.00
O_2–$2H_3O^+$	3.23	3.49	2.81	3.29

Compared with the clean CuO(111) surface, the hydrogenated surface possesses a longer O–O bond length, a higher adsorption energy and greater charge transfer, thus demonstrating better catalytic activity. Subsequent to the O_2 activation process, O_2^- ions will react with the H_3O^+ ions in solution to generate H_2O_2, as shown in Fig. 4b and d. Two H atoms originating from two H_3O^+ ions bond with one O_2^- ion to form one H_2O_2 molecule. The geometric parameters of the newly-formed H_2O_2 molecule agree well with those of the free H_2O_2 molecule. The distances between the O_2^- ion and Cu_{3C} atoms on both the clean and hydrogenated CuO surfaces are elongated (2.1 and 2.5 Å) after the formation of H_2O_2, which indicates that the formed H_2O_2 molecules depart from the CuO surfaces spontaneously. The calculated energetic pathway[50] (Fig. 5)

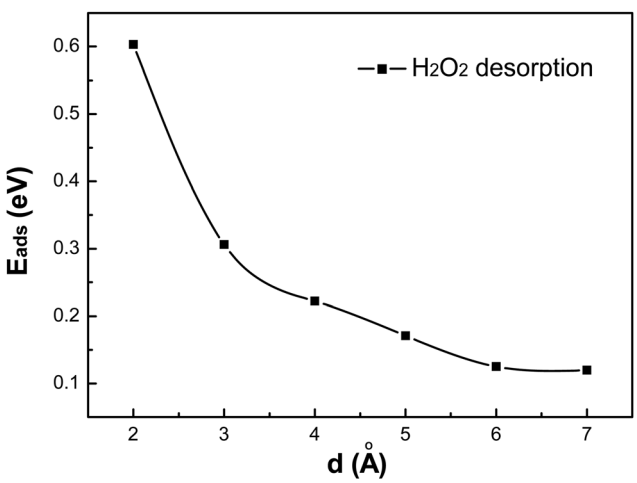

Fig. 5 Energetic pathways calculated for H_2O_2 desorption from the CuO(111) surface.

for H_2O_2 desorption on the CuO(111) surface demonstrates that the H_2O_2 desorption process is barrier-less. In the photocatalytic process, the H_2O_2 molecules produced on the CuO surfaces are adsorbed by the Cu_2O surfaces to generate $^{\bullet}OH$ radicals. The instant desorption of H_2O_2 on the CuO(111) surface will greatly increase the chances of H_2O_2 adsorption on Cu_2O(111) surface. From the calculated results, it can be concluded that for both the formation and desorption processes of H_2O_2, the hydrogenated CuO(111) surface has promotive actions which can be explained by the electrostatic interactions of surface H atoms.

To account for the feasibility of H_2O_2 production on the CuO(111) surface, we calculated the adsorption energies for a series of configurations with different initial distances from 7 Å to 2 Å between the entity (O_2 or H_3O^+) and the target (surface Cu_{3C} atoms or activated O_2^- ion). The calculated energetic pathways for two stages of the H_2O_2 formation process are shown in Fig. 6; the results indicate that the generation of H_2O_2 is barrier-less on both the clean and hydrogenated CuO(111) surfaces. In the first stage, O_2 molecules can be activated into O_2^- ions through barrier-less diffusion of O_2 to the CuO(111) surface, which is coincident with the case on the TiO_2(101) surface.[51] In the second stage, the activated O_2^- ion can react with H_3O^+ ions to form H_2O_2 molecules without any activation barrier. From Fig. 6, it can be seen that the energy released by the reaction between activated O_2^- ion and H_3O^+ ions is much larger than that of the O_2 activation, indicating that O_2 activation is much more difficult than the subsequent H_2O_2 formation reaction. Thus, O_2 activation plays a key role in the formation of H_2O_2. From the calculated energetics of O_2 activation, the hydrogenated CuO(111) surface possesses higher adsorption energy than the clean CuO(111) surface at each initial distance, showing that formation of H_2O_2 is easier after surface hydrogenation. In addition, the effective distances (where the energies change rapidly, as shown in Fig. 6) for O_2 activation and the subsequent reactions on hydrogenated surfaces are longer than those on clean surfaces. These results further confirm the promotive effect of surface H atoms on H_2O_2 formation. Therefore, it is reasonably expected that a mildly acidic water environment is beneficial for the formation of H_2O_2 on low-index CuO surfaces. Bandara *et al.*[22] reported that the maximum production of H_2O_2 occurs at pH 6.6, which presents direct evidence for our calculated results.

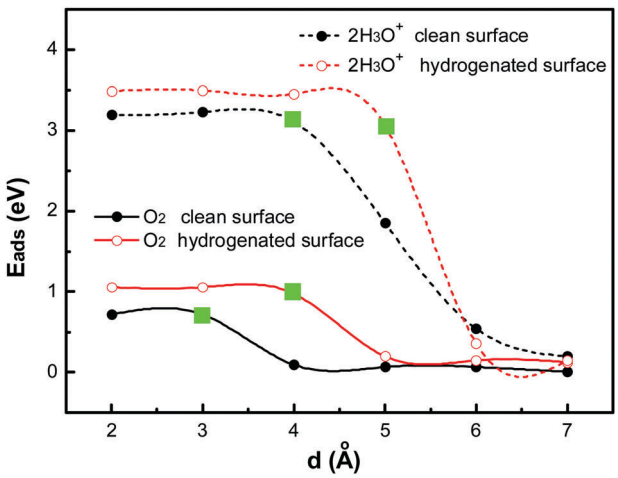

Fig. 6 Energetic pathways calculated for O_2 activation (solid line) and the reaction of $2H_3O^+$ and activated O_2^- ion (dashed line) on clean (black line) and hydrogenated (red line) CuO(111) surfaces. The *d* value indicates the initial distance between the entity (O_2 or H_3O^+) and the target (surface Cu_{3C} atoms or activated O_2^- ion). The effective distance of each pathway is marked by a green square.

Unlike the CuO(111) surface, the hydrogenated high-index surfaces, such as (311) and (202), are not thermodynamically stable owing to their high surface energies. Fortunately, the adsorption energies of O_2 on the clean CuO(311) and (202) surfaces are much higher than those of both the clean and hydrogenated (111) surfaces, as shown in Table 5. Thus, the high-index surfaces show stronger capability for O_2 activation than the CuO(111) surface, signifying that they have higher catalytic activities for the formation of H_2O_2. The enhanced catalytic activities derive from the increasing density of the active sites. In terms of the above-analyzed O_2 adsorption on the (111) surface, it is found that the O_2 activation mainly occurs on Cu_{3C} sites, which indicates that the surface Cu_{3C} atoms are the active sites for O_2 activation. The increasing number of active sites ensures the enhanced activities of the high-index surfaces. Fig. 7 displays the optimized CuO(311) and (202) surfaces, as well as the corresponding H_2O_2 formation reactions. For the CuO(311) surface, a rough plane with stepped atoms is reconstructed after optimization. The outermost Cu_{2C} atoms move 0.739 Å towards the O_{2C} atoms. The distance between the O_{2C} and Cu_{2C} atoms decreases from 2.766 to 2.027 Å, which is close enough to form a new Cu–O bond (marked by dashed lines). Thus, the exposed O_{2C} and Cu_{2C} atoms are transformed into O_{3C} (marked by green circles) and Cu_{3C} (marked by purple circles) atoms, as shown in Fig. 7a. Meanwhile, the relatively flat (202) surface is less distorted, with very slight movement of the exposed O_{3C} and Cu_{3C} atoms, as shown in Fig. 7d; therefore, it supplies many Cu_{3C} sites for O_2 activation. In addition, the formation of H_2O_2 on high-index surfaces is confirmed to be a barrier-less process. As a result, the CuO NWs with abundant exposed high-index surfaces can be expected to yield many H_2O_2 molecules, thus generating enough $^{\bullet}OH$ species to enhance the photocatalytic activity of the Cu_2O NPs/CuO NWs system.

3.3 The light excited state of the Cu_2O/CuO heterostructure

To gain an in-depth understanding of the photocatalytic system, the influence of the photoexcited Cu_2O/CuO heterostructure on the surface reactions should be taken into account. Because conventional DFT cannot predict reliable band structures for Cu_2O and CuO, the positions of the conduction band minimum (CBM) and valence band maximum (VBM) were determined by the following equations:[52]

$$E_{CBM} = \chi - E^e - 0.5E_g \quad (2)$$

$$E_{VBM} = E_g + E_{CBM} \quad (3)$$

where E_{CBM} and E_{VBM} are the potentials of the CB and VB edges, respectively, with respect to the normal hydrogen electrode

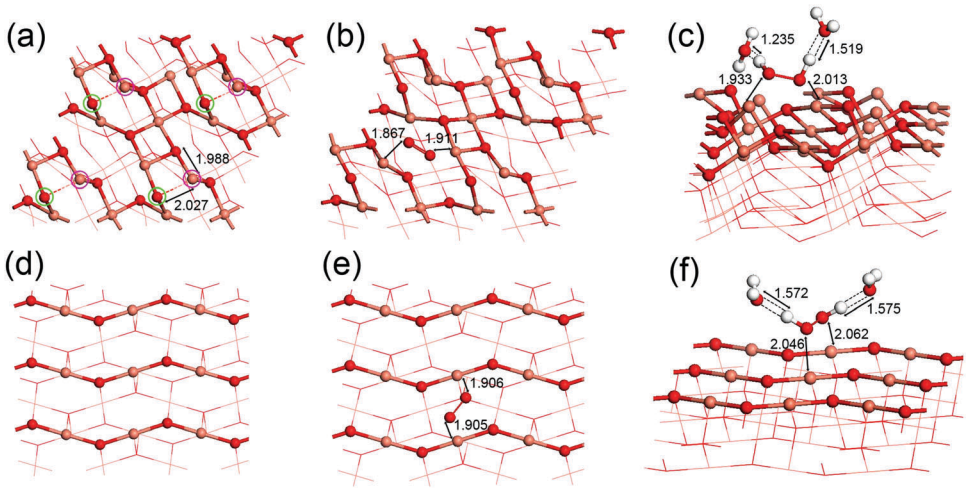

Fig. 7 Optimized clean surface (a), activation of O_2 (b) and final products (c) on CuO(311) surface; optimized clean surface (d), activation of O_2 (e) and final products (f) on CuO(202) surface. The bond lengths are given in Å.

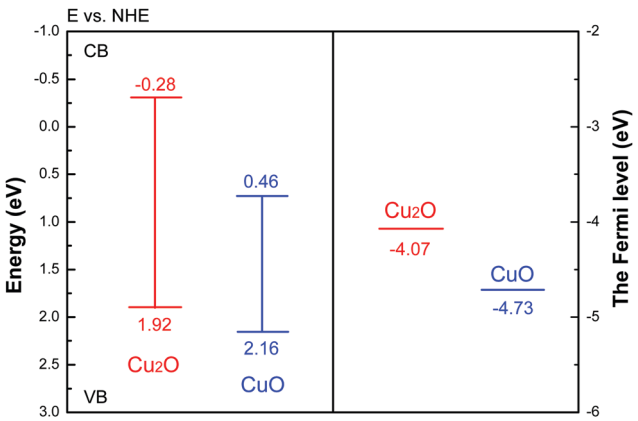

Fig. 8 The calculated CBM and VBM positions of Cu_2O and CuO with respect to NHE and their Fermi levels.

(NHE); χ is the electronegativity of the semiconductor, which is equal to the geometric mean of the electronegativities of the compositions; E^e is the energy of a free electron on the hydrogen scale (4.5 eV); and E_g is the bandgap of the semiconductor. Here, the experimental bandgaps of Cu_2O (2.2 eV) and CuO (1.7 eV) are adopted. Fig. 8 shows the calculated CBM and VBM positions and Fermi levels for Cu_2O and CuO. It can be found that both the CBM and VBM of Cu_2O are higher than those of CuO, and the order of their redox potentials is similar to that of the Fermi levels. The distinct position characteristics of CBM and VBM for CuO and Cu_2O ensure that the photogenerated electrons transfer from Cu_2O to CuO while the holes transfer from CuO to Cu_2O when the Cu_2O/CuO system is irradiated by visible light. Then, as can be imagined, positive charges accumulate in the Cu_2O NPs while negative charges migrate to the CuO NWs; thus, the positive Cu_2O NPs and negative CuO NWs are combined into the excited Cu_2O/CuO heterostructure. From the Mulliken population analysis for the H_2O_2 adsorption configurations in Table 2, it is found that the electrons transfer from the $Cu_2O(111)$ surface to H_2O_2 molecules during the dissociation process. Because the excited Cu_2O NPs are full of holes, the influence of positive Cu_2O on the dissociation of H_2O_2 is worthy of consideration. In our calculations without light irradiation, the $^\bullet$OH formation mechanism is believed to consist of two steps:

$$H_2O_2 + 2e^- \rightarrow 2OH^- \quad (4)$$

$$2OH^- + 2h^+ \rightarrow 2\,^\bullet OH \quad (5)$$

at first, H_2O_2 molecules gain electrons from the Cu_2O surface to generate OH^-, as indicated by the charge transfer analysis. Then, the generated OH^- ions react with the newly generated holes in the first step to produce $^\bullet$OH. This helps to explain the formation of $^\bullet$OH radicals by the decomposition of H_2O_2.[53] The delocalization of holes formed in the first step in eqn (4) can lead to incompletion of the second step in eqn (5). This may be the reason that the calculated magnetic moments (in Table 3) for the $^\bullet$OH species on Cu_2O are smaller than those of free $^\bullet$OH radicals. For the photoexcited system, positive Cu_2O with holes cannot provide electrons for H_2O_2 dissociation without external electron sources. However, when the OH^- ions in the solution are adsorbed on positive Cu_2O, extra electrons are introduced into the photoexcited system. Supplementary electrons can be excited to H_2O_2 and consumed to generate $^\bullet$OH radicals. The photo-generated holes on Cu_2O will promote the second step in eqn (5) to produce $^\bullet$OH radicals. In addition, H_2O_2 molecules can be dissociated by holes to generate oxidant species, such as $^\bullet$OOH.[54] Hence, it can be concluded that H_2O_2 dissociation definitely occurs on the excited Cu_2O. On the one hand, holes work to generate $^\bullet$OOH; on the other hand, electrons work to produce $^\bullet$OH. Furthermore, the experimental results suggest that a positive synergistic effect exists between the positively-charged catalyst surface and the H_2O_2 molecules.[55] Thus, H_2O_2 dissociation can take place and can even be promoted on the excited Cu_2O NPs with photogenerated holes. Meanwhile, the activation of O_2 on negative CuO will be promoted in the excited Cu_2O/CuO system according to the direction of electron transfer,

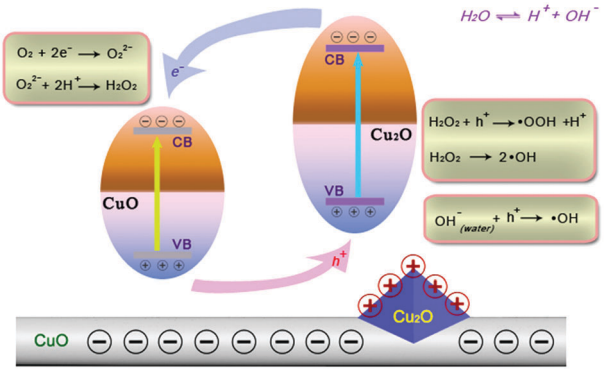

Fig. 9 Schematic for the photocatalytic formation of •OH.

resulting in enhanced H_2O_2 formation. Overall, the catalytic cycle between Cu_2O NPs and CuO NWs is well established, and the generation of oxidant species will be promoted after the light irradiation.

3.4 Photocatalytic mechanism of Cu_2O/CuO nanocomposites

Based on the calculated and experimental results above, we propose a plausible mechanism of photocatalytic generation of •OH in the Cu_2O/CuO nanocomposite system, as shown in Fig. 9. Upon visible light irradiation, Cu_2O and CuO with a narrow bandgap can absorb visible light directly to generate holes and electrons. Owing to the unique energy band structure of the Cu_2O/CuO system, the oriented migration of the photogenerated charge carriers (holes and electrons) induces the positively-charged Cu_2O NPs and the negatively-charged CuO NWs. The OH^- ions produced by water dissociation are consumed by Cu_2O NPs to generate •OH, leading to constant water dissociation throughout the photodegradation process. The remaining H^+ ions react with O_2 from the surrounding environment to form H_2O_2 on the CuO NWs. Then, the formed H_2O_2 molecules are adsorbed and dissociate on the Cu_2O NPs to produce •OH and •OOH radicals for the degradation of MO. Simply stated, the photogenerated holes and electrons in the Cu_2O/CuO heterostructure are separated and utilized efficiently by producing oxidant species, which will improve the photocatalytic performance.

4. Conclusions

In summary, the detailed photocatalytic mechanism of a Cu_2O NPs/CuO NWs hybrid nanostructure is investigated by DFT calculations. The enhanced photocatalytic efficiency is attributed to the sufficient oxidant species produced by the synergistic relationship of the Cu_2O NPs and CuO NWs in the hybrid photocatalytic system. H_2O_2 molecules self-generated on CuO NWs are dissociated into oxidant species by Cu_2O NPs. Our calculation results demonstrate that the Cu_2O(111) surfaces play a very important role in the formation of oxidant species. Owing to the different roles of Cu_2O and CuO, the constant production of oxidant species can proceed systematically during the photocatalytic degradation process. These results will provide theoretical guidance for designing appropriate photocatalytic materials with enhanced photocatalytic performance.

Acknowledgements

The authors are grateful for financial support from the National Key Basic Research Development Program of China (Grant no. 2012CB722705), the Natural Science Foundation for Outstanding Young Scientists in Shandong Province, and China (Grant no. JQ201002). Y. Q. Wang is also grateful for financial support from the Top-notch Innovative Talent Program of Qingdao City (Grant no. 13-CX-8) and the Taishan Scholar Program of Shandong Province, China. F. H. Tian is grateful for financial support from the National Natural Science Foundation of China (Grant no. 20703027), and Shandong Excellent Young Scientist Research Award Fund (Grant no.: BS2011NJ004).

References

1 M. R. Hoffmann, S. T. Martin, W. Choi and D. W. Bahnemannt, *Chem. Rev.*, 1995, **95**, 69–96.
2 S. Malato, P. Fernández-Ibáñez, M. I. Maldonado, J. Blanco and W. Gernjak, *Catal. Today*, 2009, **147**, 1–59.
3 D. Barreca, G. Carraro, V. Gombac, A. Gasparotto, C. Maccato, P. Fornasiero and E. Tondello, *Adv. Funct. Mater.*, 2011, **21**, 2611–2623.
4 K. Nakataa and A. Fujishima, *J. Photochem. Photobiol., C*, 2012, **13**, 169–189.
5 S. Sakthivel, B. Neppolian, M. V. Shankar, B. Arabindoo, M. Palanichamy and V. Murugesan, *Sol. Energy Mater. Sol. Cells*, 2003, **77**, 65–82.
6 N. D. Feng, Q. Wang, A. M. Zheng, Z. F. Zhang, J. Fan, S. B. Liu, J. P. Amoureux and F. Deng, *J. Am. Chem. Soc.*, 2013, **135**, 1607–1616.
7 A. A. Dubale, C. J. Pan, A. G. Tamirat, H. M. Chen, W. N. Su, C. H. Chen, J. Rick, D. W. Ayele, B. A. Aragaw, J. F. Lee, Y. W. Yang and B. J. Hwang, *J. Mater. Chem. A*, 2015, **3**, 12482–12499.
8 J. H. Yang, D. G. Wang, H. X. Han and C. Li, *Acc. Chem. Res.*, 2013, **46**, 1900–1909.
9 S. S. Lee, H. W. Bai, Z. Y. Liu and D. D. Sun, *Water Res.*, 2013, **47**, 4059–4073.
10 P. Massa, F. Ivorra, P. Haure and R. Fenoglio, *J. Hazard. Mater.*, 2011, **190**, 1068–1073.
11 P. Wang, X. M. Wen, R. Amal and Y. H. Ng, *RSC Adv.*, 2014, **5**, 5231–5236.
12 H. G. Yu, J. G. Yu, S. W. Liu and S. Mann, *Chem. Mater.*, 2007, **19**, 4327–4334.
13 W. Q. Fang, X. Q. Gong and H. G. Yang, *J. Phys. Chem. Lett.*, 2011, **2**, 725–734.
14 L. L. Feng, G. T. Yu, Y. Y. Wu, G. D. Li, H. Li, Y. H. Sun, T. Asefa, W. Chen and X. X. Zou, *J. Am. Chem. Soc.*, 2015, **137**, 14023–14026.
15 T. Zhu, W. L. Ong, L. L. Zhu and G. W. Ho, *Sci. Rep.*, 2015, **5**, 10601.

16 J. Fernández, J. Kiwi, J. Baeza, J. Freer, C. Lizama and H. D. Mansilla, *Appl. Catal., B*, 2004, **48**, 205–211.
17 S. Nam, V. Renganathan and P. G. Tratnyek, *Chemosphere*, 2001, **45**, 59–65.
18 L. Xu, H. Y. Xu, S. B. Wu and X. Y. Zhang, *Appl. Surf. Sci.*, 2012, **258**, 4934–4938.
19 T. Tatsuma, S. Tachibana, T. Miwa, D. A. Tryk and A. Fujishima, *J. Phys. Chem. B*, 1999, **103**, 8033–8035.
20 C. Wang, Y. Q. Wang, X. H. Liu, F. Y. Diao, L. Yuan and G. W. Zhou, *Phys. Chem. Chem. Phys.*, 2014, **16**, 17487–17492.
21 Y. M. Lin, D. Z. Li, J. H. Hu, G. C. Xiao, J. X. Wang, W. J. Li and X. Z. Fu, *J. Phys. Chem. C*, 2012, **116**, 5764–5772.
22 J. Bandara, I. Guasaquillo, P. Bowen, L. Soare, W. F. Jardim and J. Kiwi, *Langmuir*, 2005, **21**, 8554–8559.
23 B. Delley, *J. Phys. Chem.*, 1996, **100**, 6107–6110.
24 B. Delley, *J. Chem. Phys.*, 2000, **113**, 7756–7764.
25 J. P. Perdew, K. Burke and M. Ernzerhof, *Phys. Rev. Lett.*, 1996, **77**, 3865–3868.
26 Y. Inada and H. Orita, *J. Comput. Chem.*, 2008, **29**, 225–232.
27 B. Delley, *Phys. Rev. B: Condens. Matter Mater. Phys.*, 2002, **66**, 155125.
28 Z. M. Liu, L. L. Ma and A. S. M. Junaid, *J. Phys. Chem. C*, 2010, **114**, 4445–4450.
29 W. W. Zhao, F. H. Tian, X. B. Wang, L. H. Zhao, Y. Wang, A. P. Fu, S. P. Yuan, T. S. Chu, L. H. Xia, J. C. Yu and Y. B. Duan, *J. Colloid Interface Sci.*, 2014, **430**, 18–23.
30 S. J. Sun, C. Y. Li, D. S. Zhang and Y. J. Wang, *Appl. Surf. Sci.*, 2015, **333**, 229–234.
31 D. H. Wells Jr., W. N. Delgass and K. T. Thomson, *J. Chem. Phys.*, 2002, **117**, 10597–10603.
32 W. Sicking, H.-G. Korth, G. Jansen, H. de Groot and R. Sustmann, *Chem. – Eur. J.*, 2007, **13**, 4230–4245.
33 A. Martínez-Ruiz, M. G. Moreno and N. Takeuchi, *Solid State Sci.*, 2003, **5**, 291–295.
34 E. Ruiz, S. Alvarez, P. Alemany and R. A. Evarestov, *Phys. Rev. B: Condens. Matter Mater. Phys.*, 1997, **56**, 7189–7196.
35 Y. Maimaiti, M. Nolan and S. D. Elliott, *Phys. Chem. Chem. Phys.*, 2014, **16**, 3036–3046.
36 R. G. Zhang, H. Y. Liu, H. Y. Zheng, L. X. Ling, Z. Li and B. J. Wang, *Appl. Surf. Sci.*, 2011, **257**, 4787–4794.
37 G. Pelz, K. M. T. Yamada and G. Winnewisser, *J. Mol. Spectrosc.*, 1993, **159**, 507–520.
38 J. Ghijsen, L. H. Tjeng, J. van Elp, H. Eskes, J. Westerink, G. A. Sawatzky and M. T. Czyzyk, *Phys. Rev. B: Condens. Matter Mater. Phys.*, 1988, **38**, 11322–11330.
39 S. Asbrink and L. J. Norrby, *Acta Crystallogr., Sect. B: Struct. Crystallogr. Cryst. Chem.*, 1970, **26**, 8–15.
40 D. Le, S. Stolbov and T. S. Rahman, *Surf. Sci.*, 2009, **603**, 1637–1645.
41 Y. Zhang, B. Deng, T. R. Zhang, D. M. Gao and A. W. Xu, *J. Phys. Chem. C*, 2010, **114**, 5073–5079.
42 Y. M. Li, Q. Zhang and J. H. Li, *Talanta*, 2010, **83**, 162–166.
43 A. S. Ethiraj and D. J. Kang, *Nanoscale Res. Lett.*, 2012, **7**, 70.
44 A. Li, H. H. Song, J. S. Zhou, X. H. Chen and S. Y. Liu, *CrystEngComm*, 2013, **15**, 8559–8564.
45 P. Yuan, D. Q. Wu, H. P. He and Z. Y. Lin, *Appl. Surf. Sci.*, 2004, **227**, 30–39.
46 K. Eigenmann and Hs. H. Günthard, *Chem. Phys. Lett.*, 1971, **12**, 12–15.
47 C. M. Lousada, A. J. Johansson, T. Brinck and M. Jonsson, *J. Phys. Chem. C*, 2012, **116**, 9533–9543.
48 M. Anpo, M. Che, B. Fubini, E. Garrone, E. Giamello and M. C. Paganini, *Top. Catal.*, 1999, **8**, 189–198.
49 B. E. Conway, J. O'M. Bockris and H. Linton, *J. Chem. Phys.*, 1956, **24**, 834–850.
50 B. White, M. Yin, A. Hall, D. Le, S. Stolbov, T. Rahman, N. Turro and S. O'Brien, *Nano Lett.*, 2006, **6**, 2095–2098.
51 Y. F. Li and A. Selloni, *J. Am. Chem. Soc.*, 2013, **135**, 9195–9199.
52 K. N. Ding, B. Chen, Z. X. Fang and Y. F. Zhang, *Theor. Chem. Acc.*, 2013, **132**, 1352.
53 W. Xu, S. L. Zhu, Y. Q. Liang, Z. Y. Li, Z. D. Cui, X. J. Yang and A. Inoue, *Sci. Rep.*, 2015, **5**, 18125.
54 J. Shi, J. Li, X. Huang and Y. Tan, *Nano Res.*, 2011, **4**, 448–459.
55 H. Y. He, J. F. Huang, L. Y. Cao and J. P. Wu, *Desalination*, 2010, **252**, 66–70.